

## ORIGINAL ARTICLE

# Femtojoule electro-optic modulation using a silicon–organic hybrid device

Sebastian Koeber<sup>1,\*</sup>, Robert Palmer<sup>1,\*</sup>, Matthias Lauer<sup>1</sup>, Wolfgang Heni<sup>1,2</sup>, Delwin L Elder<sup>3</sup>, Dietmar Korn<sup>1</sup>, Markus Woessner<sup>1</sup>, Luca Alloatti<sup>1,4</sup>, Swen Koenig<sup>1,5</sup>, Philipp C Schindler<sup>1,5</sup>, Hui Yu<sup>6,7</sup>, Wim Bogaerts<sup>6</sup>, Larry R Dalton<sup>3</sup>, Wolfgang Freude<sup>1</sup>, Juerg Leuthold<sup>1,2</sup> and Christian Koos<sup>1</sup>

Energy-efficient electro-optic modulators are at the heart of short-reach optical interconnects, and silicon photonics is considered the leading technology for realizing such devices. However, the performance of all-silicon devices is limited by intrinsic material properties. In particular, the absence of linear electro-optic effects in silicon renders the integration of energy-efficient photonic–electronic interfaces challenging. Silicon–organic hybrid (SOH) integration can overcome these limitations by combining nanophotonic silicon waveguides with organic cladding materials, thereby offering the prospect of designing optical properties by molecular engineering. In this paper, we demonstrate an SOH Mach–Zehnder modulator with unprecedented efficiency: the 1-mm-long device consumes only  $0.7 \text{ fJ bit}^{-1}$  to generate a  $12.5 \text{ Gbit s}^{-1}$  data stream with a bit-error ratio below the threshold for hard-decision forward-error correction. This power consumption represents the lowest value demonstrated for a non-resonant Mach–Zehnder modulator in any material system. It is enabled by a novel class of organic electro-optic materials that are designed for high chromophore density and enhanced molecular orientation. The device features an electro-optic coefficient of  $r_{33} \approx 180 \text{ pm V}^{-1}$  and can be operated at data rates of up to  $40 \text{ Gbit s}^{-1}$ .

Light: Science & Applications (2015) 4, e255; doi:10.1038/lsa.2015.28; published online 27 February 2015

**Keywords:** electro-optic materials; electro-optic modulation; nonlinear organic materials; silicon-organic hybrid

## INTRODUCTION

Optical interconnects are the most promising option to overcome transmission bottlenecks in data centres and high-performance computers, and energy consumption is one of the most important parameters of the associated photonic–electronic interfaces. Targeted figures are tens of femtojoule per bit for transmitters in off-chip connections, and a few femtojoule per bit for on-chip links.<sup>1</sup> Key requirements are low drive voltages that can be provided by standard CMOS (complementary metal oxide semiconductor) circuitry without further amplification. Apart from energy efficiency, modulators need to provide fast electro-optic (EO) response along with large optical operation bandwidth to ensure high-speed transmission and flexibility in wavelength-division multiplexing systems. Moreover, dense integration is essential, calling for a small device footprint.

Silicon photonics is currently the most promising technology to realize such devices, leveraging mature high-yield CMOS processing and offering the potential of photonic–electronic co-integration on large-area silicon wafers. However, second-order nonlinearities are absent in bulk silicon due to inversion symmetry of the crystal lattice.

Hence, current silicon-based modulators<sup>2,3</sup> have to rely on free-carrier depletion or injection in p–n, p–i–n or metal-oxide-semiconductor structures. This leads to various tradeoffs when realizing fast and energy-efficient devices with small footprint: while carrier injection in forward-biased p–i–n structures enables compact modulators with voltage-length products as low<sup>4</sup> as  $U_{\pi}L=0.36 \text{ V mm}$ , free-carrier lifetime currently limits the modulation speed to  $25 \text{ Gbit s}^{-1}$  and requires strong pre-emphasis of the drive signal.<sup>5</sup> Moreover, energy efficiency of these devices is intrinsically limited to the  $\text{pJ bit}^{-1}$  range due to the permanent injection current flowing through the diode section. In contrast, carrier depletion in reverse-biased p–n junctions enables negligible bias currents and symbol rates<sup>6</sup> of up to  $50 \text{ GBd}$ , but typical voltage-length products are beyond  $10 \text{ V mm}$  and thus, much larger than those of injection-type devices. For a silicon-based Mach–Zehnder modulator (MZM), the lowest reported energy consumption amounts to  $200 \text{ fJ bit}^{-1}$ , achieved in a 5-mm-long depletion-type device.<sup>7</sup> Modulation energies and device footprint can be significantly reduced by using resonant structures such as microrings, microdiscs or photonic-crystal

<sup>1</sup>Institute of Photonics and Quantum Electronics (IPQ) and Institute of Microstructure Technology (IMT), Karlsruhe Institute of Technology (KIT), 76131 Karlsruhe, Germany; <sup>2</sup>Now with: Institute of Electromagnetic Fields, Swiss Federal Institute of Technology (ETH), Zurich, Switzerland; <sup>3</sup>University of Washington, Department of Chemistry, Seattle, WA 98195-1700, USA; <sup>4</sup>Now with: Massachusetts Institute of Technology, Research Lab of Electronics (RLE), Cambridge, MA 02139, USA; <sup>5</sup>Now with: Infinera Corporation, Sunnyvale, CA, USA; <sup>6</sup>Ghent University – IMEC, Photonics Research Group, Department of Information Technology, Gent, Belgium and <sup>7</sup>Now with: Department of Information Science and Electronic Engineering, Zhejiang University, Hangzhou 310027, China

\*These authors contributed equally to the work

Correspondence: C Koos, Institute of Photonics and Quantum Electronics (IPQ) and Institute of Microstructure Technology (IMT), Karlsruhe Institute of Technology (KIT), 76131 Karlsruhe, Germany

E-mail: christian.koos@kit.edu

received 12 August 2014; revised 12 November 2014; accepted 17 December 2014; accepted article preview online 18 December 2014

waveguides.<sup>2,8</sup> For resonant silicon-based modulators, the lowest energy consumption reported to date amounts to  $3 \text{ fJ bit}^{-1}$  and has been achieved with a microdisc device<sup>8</sup> operated at a data rate of  $12.5 \text{ Gbit s}^{-1}$ . However, the optical bandwidth of resonant devices is inherently limited, and resonance wavelengths are often subject to strong temperature-induced drifts.

Our work aims at overcoming the intrinsic limitations of all-silicon devices by combining conventional silicon-on-insulator (SOI) slot waveguides<sup>9</sup> with organic cladding materials in a hybrid approach. The concept of silicon–organic hybrid (SOH) integration<sup>10,11</sup> leverages both the benefits of large-scale standardized CMOS processing and the wealth of optical properties provided by theory-guided molecular design of organic materials.<sup>12</sup> In particular, the SOH concept lends itself to highly efficient EO modulators that feature a large modulation bandwidth, a broad range of operation wavelengths and a small device footprint.<sup>13–15</sup> First, SOH EO devices have been demonstrated using guest–host systems of polymer materials that are doped with EO molecules, so-called chromophores.<sup>16–21</sup> When used as thick layers between transparent electrodes, such materials exhibit high EO coefficients<sup>22</sup> of up to  $118 \text{ pm V}^{-1}$ . However, for nanophotonic SOH modulators, in-device EO coefficients are found to be much lower with typical values in the range<sup>15,17,23–26</sup> of  $20\text{--}60 \text{ pm V}^{-1}$ , leading to energy consumptions<sup>19</sup> of  $300 \text{ fJ bit}^{-1}$  or more. These figures are

comparable to those of all-silicon devices, but still far from exploiting the full potential of the SOH approach.

Here, we demonstrate that an ultralow energy consumption of down to  $0.7 \text{ fJ bit}^{-1}$  can be achieved on the silicon integration platform even with non-resonant devices. In a proof-of-concept experiment, a 1-mm-long SOH MZM is operated with drive voltages as small as  $80 \text{ mV}_{\text{pp}}$  at a data rate of  $12.5 \text{ Gbit s}^{-1}$  with a bit-error ratio (BER) below the threshold for hard-decision forward-error correction.<sup>27</sup> This demonstration is enabled by combining an optimized SOH slot-waveguide modulator with a novel class of organic EO materials, which consists of pure chromophores instead of a chromophore–polymer guest–host system. The modulator exhibits an in-device EO coefficient of  $180 \text{ pm V}^{-1}$ , and enables modulation with peak-to-peak drive voltages of down to  $80 \text{ mV}$  at  $12.5 \text{ Gbit s}^{-1}$ . The devices support data rates of up to  $40 \text{ Gbit s}^{-1}$  with an extinction ratio exceeding  $10 \text{ dB}$ . At DC (direct current), the  $U_{\pi}L$  product is as low as  $0.5 \text{ V mm}$ .

## MATERIALS AND METHODS

### SOH EO modulator

A schematic and a cross-sectional view of an SOH MZM are displayed in Figure 1a and 1b, respectively. The device consists of two 1-mm-long SOH phase modulators that are driven in push–pull configuration by a single coplanar transmission line with a ground–signal–ground

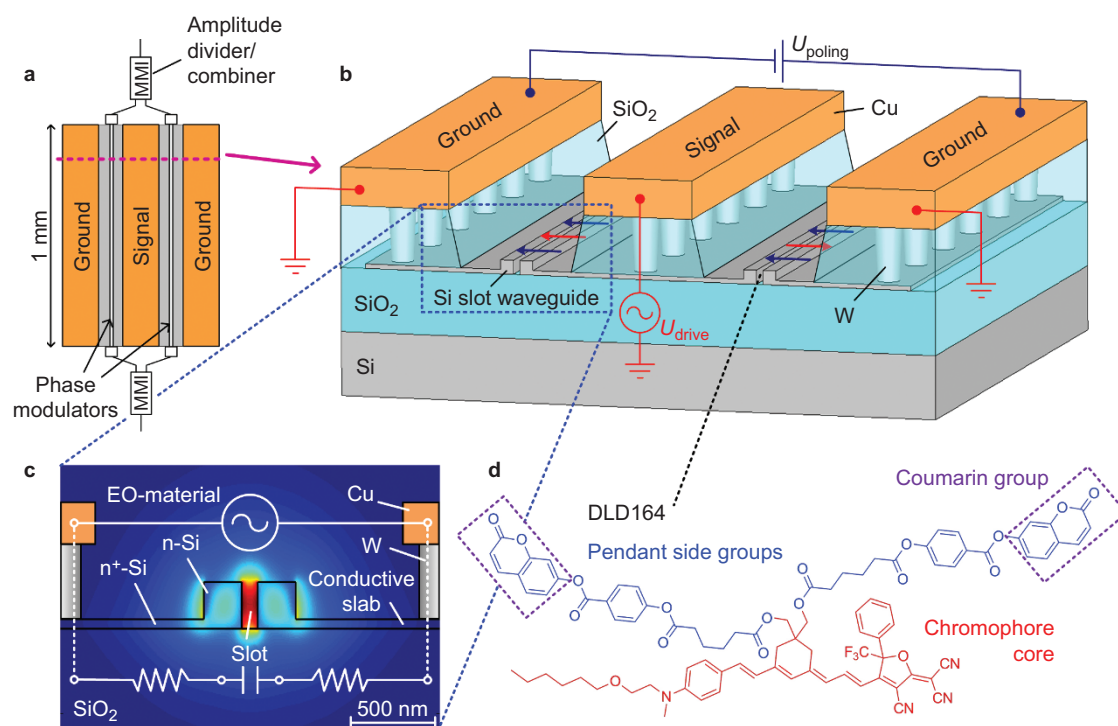


**Figure 1** Schematic of an SOH MZM. (a) Two 1-mm-long silicon slot waveguides act as phase modulators and are driven in push–pull mode by a ground–signal–ground coplanar transmission line. Further details of the photonic integrated circuit are explained in the Supplementary Information. (b) Cross-section of the MZM. The transmission line consists of 600-nm-thick copper (Cu) electrodes connected to the silicon slot waveguides by 900-nm-high tungsten (W) vias. The organic cladding (not shown) is deposited into the slot region of the SOI waveguide and is then poled at an elevated temperature by applying a poling voltage  $U_{\text{poling}}$  between the floating ground electrodes of the coplanar transmission line. This leads to a strong poling field  $E_{\text{poling}} = U_{\text{poling}}/2W_{\text{slot}}$  in each slot that aligns the dipolar chromophores as indicated by dark blue arrows. The alignment is antisymmetric with respect to the RF modulation field marked by red arrows, resulting in a push–pull operation of the MZM. (c) Schematic and simulated quasi-TE optical mode of a slot waveguide that is filled with an EO organic material. The two rails of the slot waveguide are connected to the transmission line by 60-nm-thick n-doped silicon slabs. The optical mode and the RF modulation field are both well confined to the slot region. This leads to strong EO interactions and therefore to a high modulation efficiency. (d) Chemical structure of the EO cladding material<sup>22</sup> DLD164. The molecule consists of a ‘ring-locked’ EO chromophore core (red), and two coumarin-based pendant side chains (blue). EO, electro-optic; MZM, Mach–Zehnder modulator; RF, radio frequency; SOH, silicon–organic hybrid; SOI, silicon-on-insulator; TE, transverse electric.

configuration. A cross-sectional view of a single SOH phase modulator is depicted in Figure 1c along with the electric field profile of the fundamental quasi-TE (quasi-transverse-electric) mode. The phase modulator section consists of an SOI slot waveguide that comprises two silicon rails separated by a 160 nm wide slot. The waveguide is covered and the slot is filled with an organic EO material that is deposited by spin coating. The rails of the slot waveguide are electrically connected to a copper radio frequency (RF) transmission line by thin n-doped silicon slabs and tungsten vias. A voltage applied to the transmission line thus drops across the narrow slot, resulting in a strong modulation field that has a large overlap with the guided optical mode.

For high-modulation efficiency, an organic material featuring a large macroscopic EO coefficient  $r_{33}$  is essential. Besides the optical properties of the individual chromophore molecule, the macroscopic EO coefficient depends on the orientation of the chromophore ensemble with respect to the modulating RF field. After deposition of the organic material, the EO coefficient is zero ( $r_{33}=0$ ) due to the random orientation of the dipolar chromophores. For achieving a non-centrosymmetric orientation (acentric order), the material must be poled. This is achieved by heating the organic material close to its glass-transition temperature  $T_g$  while applying an external electric field to align the dipolar chromophore molecules. The material is subsequently cooled back to room temperature while maintaining the poling field, thereby conserving the acentric order of the chromophores and the macroscopic EO coefficient of the material. For poling of our device, we apply the poling voltage  $U_{\text{poling}}$  between the two floating ground electrodes of the RF transmission line,<sup>19</sup> as depicted in Figure 1b. This way, half of the poling voltage drops across each silicon slot, resulting in an orientation of the dipolar chromophores (dark blue arrows), which is parallel to the RF modulation field (red arrows) in the left half of the ground–signal–ground transmission line and anti-parallel in the right half. This leads to a positive phase shift in the left arm of the MZM, and to a negative phase shift in the right arm, thereby resulting in push–pull operation of the device.

The optical fiber-to-fiber insertion loss of the modulator amounts to 16.5 dB, dominated by fiber-to-chip coupling losses of the non-optimized grating couplers<sup>28</sup> of approximately 10.5 dB for both interfaces. The on-chip loss of the device is approximately 6 dB for maximum transmission of the modulator and is dominated by scattering losses due to sidewall roughness in the slot waveguides. A more detailed breakdown of the on-chip insertion losses can be found in Supplementary Information. A reduction of sidewall roughness by optimization of the fabrication process and shorter device lengths is expected to enable SOH MZM with on-chip insertion losses below 2 dB.

### Organic material with increased EO activity

In general, the EO coefficient of the organic cladding depends on the nonlinear polarizability of a single chromophore molecule, on the volume concentration of the chromophores in the material, and on the average orientation of the molecules with respect to the applied electric field.<sup>29</sup> This leads to an expression<sup>30</sup> of the form

$$r_{33} = -2\beta_{zzz}N\langle\cos^3\theta\rangle\frac{g}{n^4} \quad (1)$$

where  $\beta_{zzz}$  denotes the first-order hyperpolarizability of the molecule along its dipole axis and  $N$  is the chromophore volume number density. For a single chromophore molecule, the quantity  $\theta$  denotes the angle between the molecular dipole axis  $z$  and the direction of the external electric field, and the average degree of chromophore orientation is described by the ensemble average  $\langle\cos^3\theta\rangle$ , the so-called

acentric order parameter. The quantity  $g$  denotes the Lorentz–Onsager local field factor<sup>12</sup> that accounts for partial field screening in the material, and  $n$  is the refractive index. Based on Equation (1), the EO coefficient can be enhanced in three ways: first, by increasing the chromophore hyperpolarizability  $\beta_{zzz}$ , second, by maximizing the chromophore density  $N$ , and third, by inducing the highest possible acentric orientation  $\langle\cos^3\theta\rangle$ .

Chromophore hyperpolarizability  $\beta_{zzz}$  has continuously been increased over the last years, driven by the advancement of computational methods that allow to theoretically predict the hyperpolarizability of molecular structures.<sup>12,30,31</sup> However, chromophore density  $N$  and average acentric orientation  $\langle\cos^3\theta\rangle$  are coupled quantities that cannot be maximized independently:<sup>12</sup> increasing chromophore density leads to strong electrostatic interactions between the dipoles, thereby counteracting the desired acentric orientation of the ensemble. For high densities, these intermolecular interactions lead to partial crystallization of the material, to vanishing EO activity and to increased scattering loss. The conventional approach to mitigate these interactions is based on using a small chromophore load of typically less than 25 wt-% in a polymer host matrix. SOH integration was so far largely based on these guest–host systems,<sup>15,17,23–25,32,33</sup> for which in-device EO coefficients were far below values achieved for parallel-plate poling of bulk reference samples. The incomplete transfer of EO coefficients from bulk materials to devices appears to be a general problem, which does not only occur in SOH devices: EO coefficients of up to 450 pm V<sup>-1</sup> can be achieved in bulk materials,<sup>12</sup> whereas the highest reported in-device EO coefficients amount to  $r_{33}=59$  pm V<sup>-1</sup> for SOH devices<sup>26</sup> and to  $r_{33}=138$  pm V<sup>-1</sup> for an all-polymer MZM.<sup>34</sup>

In our experiments, the constraints of low in-device EO coefficients are overcome by using the novel monolithic organic material DLD164. The design of the molecule allows to simultaneously increase the chromophore density  $N$  and acentric orientation  $\langle\cos^3\theta\rangle$ . The chemical structure of DLD164 is depicted in Figure 1d and its synthesis is reported in Ref. 22. The chromophore molecules are designed to have an EO active core (marked in red) with pendant coumarin-containing side groups (marked in blue). The interaction of these side groups effectively suppresses head-to-tail orientation of the dipolar chromophores and thus inhibits partial crystallization of the material. For a more detailed discussion on this principle, the reader is referred to Refs. 22, 35 and 36. This approach allows for applying the neat chromophore as cladding material without the need for an insulating polymer matrix. Moreover, as discussed in Ref. 35, the intermolecular interaction of the coumarin-pendant side groups reduces the number of rotational degrees of freedom of the chromophores from three to two. Based on a theoretical model, this interaction increases the average acentric order  $\langle\cos^3\theta\rangle$  by a factor of 2, due to a lower poling energy required to achieve a given average chromophore orientation, see Ref. 36 for a more detailed discussion of this effect.

## RESULTS AND DISCUSSION

### Poling of the organic material and DC characterization

SOI waveguides are fabricated by standard CMOS processes using optical lithography, and EO materials are deposited by spin coating (see Supplementary Information for a more detailed description). The EO coefficient of the cladding after poling is studied by measuring the voltage-dependent transmission of an MZM at DC (Figure 2a). The depicted trace refers to a 1-mm-long device which was poled by a voltage of 40 V per phase modulator section. This corresponds to a remarkably high poling field of  $E_{\text{poling}}\approx 250$  V  $\mu\text{m}^{-1}$  in the

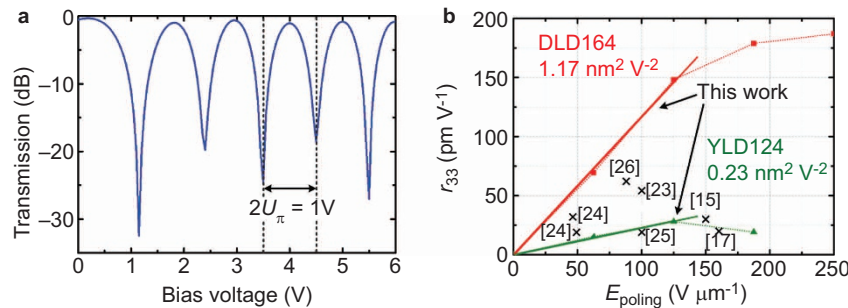


**Figure 2** Static characterization of SOH MZM. (a) Transmission vs. applied DC voltage at a wavelength of 1546 nm for a 1-mm-long SOH MZM in push–pull configuration. At a bias of 4 V, we find a  $\pi$ -voltage of  $U_\pi=0.5$  V. For zero bias, free charges in the cladding lead to partial field screening of the applied fields, which leads to increased  $\pi$ -voltages. (b) EO coefficient  $r_{33}$  vs. poling field  $E_{\text{poling}}$  for a monolithic chromophore cladding (DLD164, red) and for a guest–host cladding containing 25 wt-% YLD124 in a PMMA matrix (green). For weak poling fields,  $r_{33}$  increases linearly with the poling field, as indicated by fitted straight lines. DLD164 reveals a poling efficiency of  $r_{33}/E_{\text{poling}}=1.17\text{ nm}^2\text{ V}^{-2}$  which is significantly higher than the value of  $0.23\text{ nm}^2\text{ V}^{-2}$  obtained for the YLD124/PMMA guest-host cladding. Crosses mark previously reported values for chromophore-doped polymers.<sup>15,17,23–26</sup> For the YLD124/PMMA guest-host cladding, breakdown occurs at field strengths exceeding  $200\text{ V}\mu\text{m}^{-1}$ , whereas DLD164 withstands all applied voltages, leading to an EO coefficient  $r_{33}$  of up to  $180\text{ pm V}^{-1}$ . EO, electro-optic; MZM, Mach–Zehnder modulator; SOH, silicon–organic hybrid.

160-nm-wide slots. The ability to withstand extraordinarily high poling fields appears to be a beneficial result of the SOH slot waveguide structure—for a bulk reference sample of monolithic organic cladding material, dielectric breakdown was already observed<sup>22</sup> at  $75\text{ V}\mu\text{m}^{-1}$ . We attribute the improved stability to thin-film effects and to a low defect probability in the slot region. The devices are characterized at infrared telecommunication wavelengths around 1550 nm. The 1-mm-long device reveals a  $\pi$ -voltage of  $U_\pi=0.5$  V measured at DC under a 4 V bias. The bias avoids partial field screening by free charges in the cladding that may occur at small DC fields<sup>37</sup> (Figure 2a). The corresponding voltage–length product amounts to  $U_\pi L=0.5\text{ V mm}$  at an optical insertion loss of 6 dB. This is a very promising result, especially when comparing the SOH MZM to a typical carrier-depletion all-silicon modulator<sup>38</sup> that features a  $\pi$ -voltage of  $U_\pi=3.1$  V at a length of 6 mm and an insertion loss of 9 dB. Taking into account the measured waveguide dimensions and the associated overlap between optical mode and RF field, we can derive the in-device EO coefficient of the cladding to be  $r_{33}=180\pm 20\text{ pm V}^{-1}$  (see Supplementary Information for details of the calculation). This coefficient clearly exceeds the maximum value of  $r_{33}=137\text{ pm V}^{-1}$  previously achieved in the corresponding bulk material reference,<sup>22</sup> where poling fields were limited by dielectric breakdown.

To verify that the extraordinarily high in-device EO coefficient is in agreement with theoretical predictions, we compare the poling efficiency  $r_{33}/E_{\text{poling}}$  of the DLD164 cladding with that of the guest–host cladding YLD124 (25 wt-%) in PMMA (polymethyl methacrylate) using nominally identical SOI waveguide structures. In terms of molecular hyperpolarizability  $\beta_{zzz}$ , the chromophore cores of DLD164 and YLD124 are identical. However, by utilizing the neat chromophore DLD164, we achieve a 2.3 times higher number density  $N$  of EO active dipoles as compared to the commonly used mixture of 25 wt-% YLD124 in PMMA (see Supplementary Information for details). For comparison of the acentric order parameters in both materials, we derive the EO coefficients  $r_{33}$  for various poling fields (Figure 2b). For weak poling fields, the EO coefficient increases linearly with  $E_{\text{poling}}$ . From the measurements, we deduce a poling efficiency of  $r_{33}/E_{\text{poling}}=1.17\text{ nm}^2\text{ V}^{-2}$  for the DLD164 material and of  $0.23\text{ nm}^2\text{ V}^{-2}$  for the YLD124/PMMA composite. Using Equation (1), we find that the product  $N<\cos^3\theta>$  for DLD164 is increased by a factor of 4.8 as compared to YLD124/PMMA: The calculated quantities  $\beta_{zzz}$  are equal in both cases, while the  $g/n^4$  ratio for YLD124/

PMMA is larger by a factor of 1.07 compared to DLD164.<sup>22</sup> Considering the 2.3-fold higher chromophore concentration  $N$ , we conclude that the acentric order parameter  $<\cos^3\theta>$  for DLD164 must be a factor 2.1 times larger than that of the YLD124/PMMA composite, which is in excellent agreement with theoretical predictions.<sup>36</sup> These findings are also consistent with independent experimental investigations of an identical chromophore concept in parallel-plate poled reference measurements,<sup>35</sup> revealing enhancements of the acentric order parameter  $<\cos^3\theta>$  by a factor 2.1 when using coumarin-based pendant side groups. We hence conclude that the concept of reduced dimensionality through harnessing engineered intermolecular interactions can be directly transferred from parallel-plate poled reference samples to devices and allows to significantly enhancing the performance of SOH devices.

### Data transmission and energy consumption

The fabricated SOH modulators were tested in transmission experiments using a non-return-to-zero (NRZ) on–off keying format. We perform two sets of experiments, aiming at modulation with lowest possible energy consumption, or with highest possible data rate. Both experiments were performed at a wavelength of 1546 nm. For the low-energy experiments we use a 1-mm-long device operated at data rates of  $12.5\text{ Gbit s}^{-1}$  and  $25\text{ Gbit s}^{-1}$ ; for the high-speed experiments, we use also devices as short as  $250\mu\text{m}$ . The corresponding experimental set-up is sketched in Figure 3a and is explained in more detail in the Supplementary Information along with the models that are used for estimating the dissipated energy per bit.

For the low-energy experiments, we operate the MZM in different driving modes and measure the BER along with the energy consumption per bit as a function of drive voltage (Figure 3b and 3c). For high data rates beyond  $20\text{ Gbit s}^{-1}$ , the 1-mm-long device acts as a travelling-wave modulator and the transmission line needs to be terminated by a matched load resistor of  $R_L=50\Omega$  to avoid detrimental back-reflections of the RF wave (Figure 3d). In this case, the RF power is dissipated along the lossy transmission line and in the termination. For a mean-free drive signal switching between  $-U_{\text{drive}}/2$  and  $+U_{\text{drive}}/2$ , the energy per bit  $W_{\text{bit}}$  is obtained by dividing the dissipated average power by the data rate  $r$ ,  $W_{\text{bit}}=(U_{\text{drive}}/2)^2/(R_L\times r)$ .

For data rates below  $20\text{ Gbit s}^{-1}$ , the modulator is much shorter than the RF wavelengths, and the device acts as a ‘lumped’ element. In this case, the MZM may be operated without termination (Figure 3e).

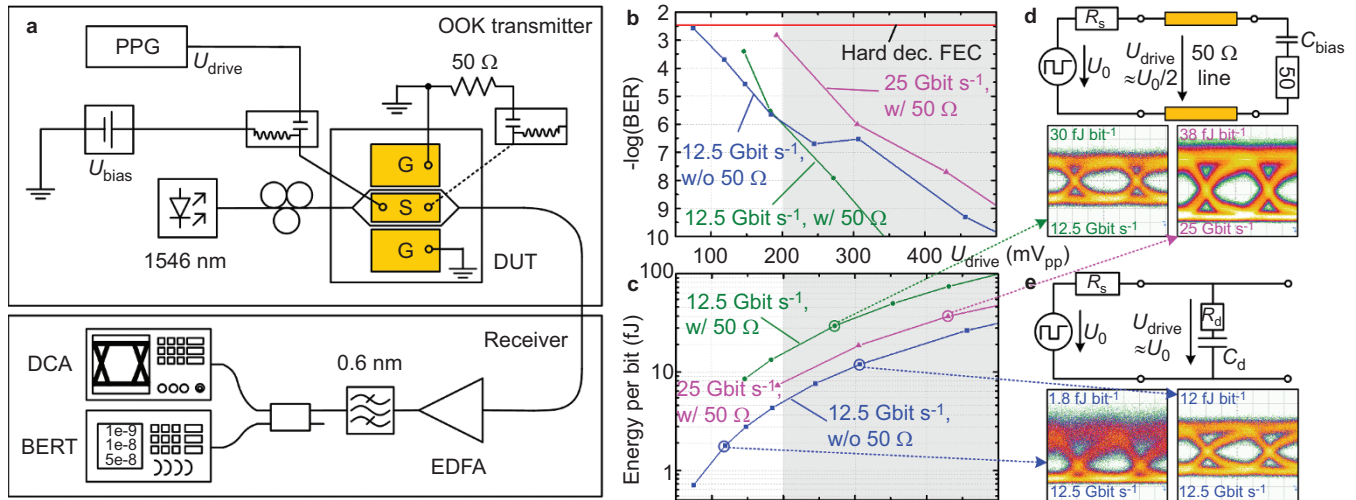


**Figure 3** Data generation and reception at lowest energy consumption. **(a)** Experimental set-up for transmission experiments. A PPG is used to drive the modulator without additional RF amplifier. The drive signal is fed to the DUT by using a GSG RF probe. A bias-T is used to adjust the operating point. A second RF probe at the end of the modulator can be used to terminate the device. Light from an external-cavity laser is coupled to the MZM using grating couplers. The modulated light is amplified by an EDFA and detected by a DCA and a BERT. **(b)** Measured BER as a function of drive voltage.<sup>27</sup> For transmission at 25 Gbit s<sup>-1</sup> (magenta), the DUT is always terminated by a 50 Ω load, whereas for a rate of 12.5 Gbit s<sup>-1</sup>, the device is driven with (green) and without (blue) termination. Data points in the gray-shaded areas were measured at the quadrature operating point of the device. **(c)** Corresponding energy per bit for the various drive voltages<sup>27</sup> of **(b)**. **(d)** Equivalent circuit of the terminated traveling-wave modulator along with the corresponding eye diagrams measured at the quadrature operating point at 25 Gbit s<sup>-1</sup> ( $U_{\text{drive}}=430$  mV<sub>pp</sub>,  $W_{\text{bit}}=38$  fJ) and at 12.5 Gbit s<sup>-1</sup> ( $U_{\text{drive}}=270$  mV<sub>pp</sub>,  $W_{\text{bit}}=30$  fJ). The internal resistance of the source and the terminating impedance amount to  $R_s=R_L=50$  Ω. **(e)** Eye diagrams at 12.5 Gbit s<sup>-1</sup> of a non-terminated device<sup>27</sup> along with the respective equivalent lumped-element circuit. The right inset shows an eye diagram at  $U_{\text{drive}}=310$  mV<sub>pp</sub> ( $W_{\text{bit}}=12$  fJ) when operating the MZM at the quadrature point. The left inset shows an eye diagram at  $U_{\text{drive}}=120$  mV<sub>pp</sub> ( $W_{\text{bit}}=1.8$  fJ) when operating below the quadrature point. BER, bit-error ratio; BERT, bit-error-ratio tester; DCA, digital communications analyzer; DUT, device under test; EDFA, erbium-doped fiber amplifier; FEC, forward-error correction; GSG, ground-signal-ground; MZM, Mach-Zehnder modulator; OOK, on-off keying; PPG, pseudo-random pattern generator; RF, radio frequency.

This significantly decreases the energy consumption, since the drive signal is no longer dissipated in a 50-Ω termination.<sup>39</sup> Instead, energy consumption is now dominated by ohmic losses that occur in the internal resistor  $R_s$  of the source and in the series resistor  $R_d$  of the device during charging and de-charging of the capacitor<sup>1</sup>  $C_d$  (see Figure 3e for an equivalent-circuit model). For a terminated device, the drive voltage  $U_{\text{drive}}$  is half the open-circuit voltage  $U_0$  of the 50-Ω source, whereas for the non-terminated device, the drive voltage  $U_{\text{drive}}$  can approach the full open-circuit voltage (see equivalent circuit in Figure 3e). This effect must be taken into account when calculating the drive voltage and the associated energy consumption of the terminated and non-terminated device. Moreover, the device capacitance  $C_d$  is an important parameter for estimating the energy consumption of the unterminated modulator. The device capacitance can be measured using a vector network analyzer, leading, e.g., to a value of  $C_d=(400\pm 20)$  fF for a 1-mm-long device (see Supplementary Information for a more detailed description of the measurement). The measured results are in good agreement with the values predicted by electrostatic simulations (CST Microwave Studio). In general, the device capacitance  $C_d$  is a frequency-dependent quantity due to its dispersive dielectric. When calculating the energy consumption, this can be taken into account by integration over the dissipated power spectrum in the frequency domain (see Supplementary Information).

For small data rates far below the 3 dB cutoff frequency of the modulator, power dissipation associated with charging/de-charging the capacitor  $C_d$  from an initial voltage 0 V to a final voltage  $U_{\text{drive}}=U_0$  and *vice versa* is independent of the series resistance and amounts to  $^1 C_d U_0^2/2$ . When driving a modulator with a digital NRZ signal, we need to take into account that charging and de-charging only occurs during 1–0 and 0–1 transitions, but not for 0–0 and 1–1 sequences. On average, charging or de-charging of the capacitor

occurs every second bit, and the energy consumption per bit hence amounts to  $^1 W_{\text{bit}}=C_d U_0^2/4$ . For data rates  $r$  approaching the 3 dB cutoff frequency of the modulator, however, the device capacitor is no longer fully charged within the timeslot of one symbol, and the energy consumption can no longer be calculated by the simple expression  $W_{\text{bit}}=C_d U_0^2/4$ . Instead, the dissipated power has to be computed for each frequency component of the NRZ power spectrum separately. The total dissipated power is then obtained by integrating over the corresponding power spectrum (see Supplementary Information for a more detailed description). For a frequency-independent device capacitance  $C_d$ , this leads to an expression of the form

$$W_{\text{bit}} = \frac{1}{4} C_d U_0^2 [1 - e^{-T/\tau}] \quad (2)$$

In this expression,  $T=1/r$  denotes the symbol duration,  $\tau=(R_s+R_d)C_d$  is the resistance-capacitance time constant of the circuit, and  $R_s$  and  $R_d$  are the series resistances of the source and of the device, as defined in Figure 3e. This model can be extended to the case of a frequency-dependent capacitance  $C_d$  (see Supplementary Information). In addition to the low-frequency approximation and the exact frequency-domain model, we also investigate a slightly simplified method based on a time-domain approximation. We find good agreement between the various methods for estimating the energy consumption of our devices and hence conclude that the results are reliable (see Supplementary Information).

For transmission at 12.5 Gbit s<sup>-1</sup>, we measure comparable BER for the terminated and non-terminated device at small drive voltages (Figure 3b and 3c). The associated energy consumption, however, is significantly lower for the non-terminated device. A drive voltage of only 80 mV<sub>pp</sub> is required to keep the measured BER below the

hard-decision forward-error correction threshold<sup>40</sup> of  $4.5 \times 10^{-3}$ , corresponding to an energy consumption of  $0.7 \text{ fJ bit}^{-1}$ . For remaining at a BER below  $10^{-9}$ , we find a drive voltage of  $U_{\text{drive}} = 460 \text{ mV}_{\text{pp}}$  ( $27 \text{ fJ bit}^{-1}$ ) for the non-terminated MZM and  $U_{\text{drive}} = 300 \text{ mV}_{\text{pp}}$  ( $40 \text{ fJ bit}^{-1}$ ) for the terminated MZM. These energy consumptions are one to two orders of magnitude below the  $200 \text{ fJ bit}^{-1}$  which were previously demonstrated for a 5-mm-long silicon-based MZM<sup>7</sup> operated at  $630 \text{ mV}_{\text{pp}}$ . The performance of our MZM is even comparable to best-in-class resonant structures,<sup>2,8</sup> where  $3 \text{ fJ bit}^{-1}$  were reported at drive voltages of  $1 \text{ V}_{\text{pp}}$ . For transmission at  $25 \text{ Gbit s}^{-1}$ , slightly worse BER are measured, and the energy consumption amounts to  $7 \text{ fJ bit}^{-1}$  ( $190 \text{ mV}_{\text{pp}}$ ) at a BER of  $4.5 \times 10^{-3}$  and to  $52 \text{ fJ bit}^{-1}$  for a BER of  $10^{-9}$ . These figures do not include the energy consumption of any external components, such as laser, optical amplifier and electrical drivers. Currents flowing due to DC voltages are measured to be below  $2 \text{ nA}$ , contributing only a negligible amount of energy ( $< 1 \text{ aJ bit}^{-1}$ ) to the budget.

For the high-speed transmission experiments at data rates of up to  $40 \text{ Gbit s}^{-1}$ , we use  $500\text{-}\mu\text{m}$ -long and  $1\text{-mm}$ -long terminated devices and a  $250\text{-}\mu\text{m}$ -long non-terminated device. For the  $1\text{-mm}$ -long device, optimum signal quality at  $12.5 \text{ Gbit s}^{-1}$  was obtained for a peak-to-peak drive voltage swing of  $U_{\text{drive}} = 950 \text{ mV}_{\text{pp}}$  measured at the output of the pulse-pattern generator. This voltage was also used for the other data rates to facilitate comparison. Note that, due to slight overmodulation and due to the frequency response of the device and the deployed RF components, the drive voltage swing is bigger than  $500 \text{ mV}_{\text{pp}}$  that would be expected from the DC voltage-length product of  $U_{\pi}L = 0.5 \text{ Vmm}$ . Eye diagrams for various data rates are depicted in

Figure 4a. The extinction ratios exceed  $10 \text{ dB}$  in all cases. At  $12.5 \text{ Gbit s}^{-1}$  and  $30 \text{ Gbit s}^{-1}$ , we measure excellent  $Q^2$ -factors of  $22 \text{ dB}$  and  $19 \text{ dB}$ , respectively, and obtain error-free operation with BER values below  $10^{-12}$ . At  $40 \text{ Gbit s}^{-1}$ , we measure a  $Q^2$  of  $15 \text{ dB}$  and a reasonably low BER of  $1 \times 10^{-8}$ . We demonstrate that  $40 \text{ Gbit s}^{-1}$  data rates can also be generated with  $500\text{-}\mu\text{m}$ -long terminated MZM and with  $250\text{-}\mu\text{m}$ -long non-terminated MZM, which were operated with drive voltages of  $U_{\text{drive}} = 2 \text{ V}_{\text{pp}}$  and  $U_{\text{drive}} = 3.4 \text{ V}_{\text{pp}}$ , respectively. These findings demonstrate that SOH modulators support data rates comparable to those of carrier-depletion p-n modulators while featuring small device footprints comparable to those of carrier-injection p-i-n modulators.

## CONCLUSIONS

We have shown that SOH integration offers the potential to implement EO devices with unprecedented performance while maintaining many of the advantages of standardized large-scale CMOS processing. We experimentally demonstrate non-resonant EO modulation at  $12.5 \text{ Gbit s}^{-1}$  with a peak-to-peak voltage swing of  $80 \text{ mV}$  and an energy consumption as small as  $0.7 \text{ fJ bit}^{-1}$ . The in-device EO coefficient of the organic cladding amounts to  $r_{33} = 180 \pm 20 \text{ pm V}^{-1}$  and is significantly larger than the values that can be achieved by parallel-plate poling of the corresponding bulk material. Moreover, our SOH modulators feature small footprint and are capable of operating at  $40 \text{ Gbit s}^{-1}$ . Our findings demonstrate that SOH integration allows overcoming intrinsic limitations of all-silicon devices: the concept combines low  $U_{\pi}L$  products comparable to those of carrier-injection devices with large EO bandwidths known from carrier-depletion

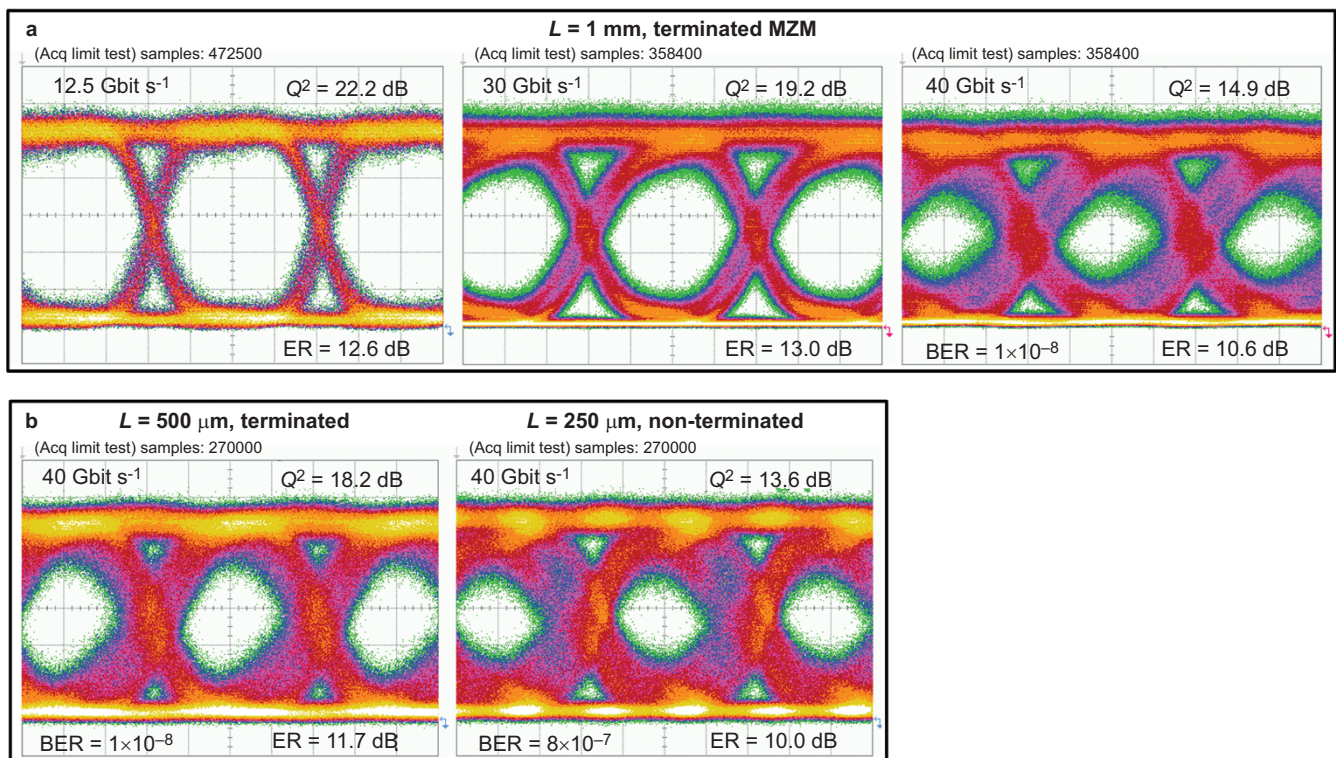


**Figure 4** High-speed modulation. (a) NRZ OOK eye diagrams<sup>27</sup> of a 1-mm-long modulator for data rates of  $12.5 \text{ Gbit s}^{-1}$ ,  $30 \text{ Gbit s}^{-1}$  and  $40 \text{ Gbit s}^{-1}$ . The modulator is biased at the quadrature point. The drive voltage is  $950 \text{ mV}_{\text{pp}}$  in all cases. The ERs exceed  $10 \text{ dB}$  even at  $40 \text{ Gbit s}^{-1}$ . Up to  $35 \text{ Gbit s}^{-1}$ , the BER is below  $10^{-12}$ . At  $40 \text{ Gbit s}^{-1}$ , we measure a low BER of  $1 \times 10^{-8}$ . (b)  $40 \text{ Gbit s}^{-1}$  eye diagrams of a  $500\text{-}\mu\text{m}$ -long terminated modulator ( $U_{\text{drive}} = 2 \text{ V}_{\text{pp}}$ ) and of a  $250\text{-}\mu\text{m}$ -long modulator without termination ( $U_{\text{drive}} = 3.4 \text{ V}_{\text{pp}}$ ). Measured  $Q^2$  factors, ER and BER are denoted in the respective figures. The pseudo-random binary sequence length is  $2^{31} - 1$ . BER, bit-error ratio; ER, extinction ratio; MZM, Mach-Zehnder modulator; NRZ, non-return-to-zero; OOK, on-off keying.

devices, while the energy consumption is less by at least one order of magnitude. We believe that there is still significant room for enhancing the performance of SOH modulators, e.g., by taking advantage of the continuously improving EO cladding materials.

One important aspect of organic EO materials is the long-term stability, both regarding thermal and photo-induced degradation. Within the experiments of this paper, we have not encountered any photo-degradation or bleaching effects, even when operating the device at input powers of more than 15 dBm, which corresponds to an intensity of  $3 \times 10^6 \text{ W cm}^{-2}$  in the slot of the SOH modulators. At higher power levels, thermal effects were already beginning to impair the performance of the device. We hence believe that material stability in our device is governed exclusively by thermal reorientation of chromophores. The glass transition temperature of the currently used DLD164 amounts to  $T_g = 66 \text{ }^\circ\text{C}$ , and thermally activated re-orientation of the chromophores reduces the lifetime of the current devices to roughly a month under ambient laboratory conditions. However, we have recently demonstrated that electro-optic coefficients of up to  $230 \text{ pm V}^{-1}$  can also be achieved by other material systems such as binary-chromophore organic glasses that combine shape-engineered dendritic molecular structures with conventional bare donor–acceptor species.<sup>37</sup> These materials feature glass transition temperatures of more than  $100 \text{ }^\circ\text{C}$  and are expected to exhibit better thermal stability. In addition, we expect that stability can be significantly improved by synthetically modified DLD164 chromophores that bear specific cross-linking agents for post-poling lattice hardening. The viability of this approach has already been demonstrated for similar classes<sup>41,42</sup> of EO compounds, with materials being stable for temperatures of up to  $250 \text{ }^\circ\text{C}$ . It has been demonstrated experimentally that these techniques can be applied to realize temperature-stable all-polymeric MZM.<sup>34</sup> Whereas earlier demonstrations of crosslinking have led to increased optical losses by absorption or scattering in the organic material, it has recently been demonstrated that this problem can be overcome by utilizing cycloaddition reactions (Diels–Alder and related cycloadditions) that do not produce chemical side products or lead to lattice distortion. In these experiments, no increase in loss has been observed in the near infrared,<sup>43</sup> and the values obtained for the glass transition temperatures after crosslinking are above  $200 \text{ }^\circ\text{C}$ .<sup>44</sup> For DLD164, the addition of crosslinking agents to the side groups can be realized without affecting the EO activity of the chromophore or the coumarin–coumarin interaction of the side chains. Thermal stability and photo-degradation of SOH devices is subject to ongoing research.

## ACKNOWLEDGEMENTS

This work was supported by the European Research Council (ERC Starting Grant ‘EnTeraPIC’, number 280145), by the Alfried Krupp von Bohlen und Halbach Foundation, and by the Initiative and Networking Fund of the Helmholtz Association. We further acknowledge support by the DFG Center for Functional Nanostructures, by the Karlsruhe International Research School on Teratronics, by the Karlsruhe School of Optics and Photonics, by the Karlsruhe Nano-Micro Facility, by the DFG Major Research Instrumentation Programme and by the EU-FP7 projects PHOXTROT and BigPIPES, by Deutsche Forschungsgemeinschaft and by the Open Access Publishing Fund of Karlsruhe Institute of Technology. Further financial support was obtained from the National Science Foundation (DMR-0905686, DMR-0120967) and the Air Force Office of Scientific Research (FA9550-09-1-0682). Silicon-on-insulator waveguides were fabricated by the European silicon photonics platform ePIXfab. Peter Johnston (University of Washington) is acknowledged for the synthesis of YLD124.

- 1 Miller DA. Energy consumption in optical modulators for interconnects. *Opt Express* 2012; **20**: A293–A308.
- 2 Reed GT, Mashanovich G, Gardes FY, Thomson DJ. Silicon optical modulators. *Nat Photonics* 2010; **4**: 518–526.
- 3 Fujikata J, Ushida J, Nakamura T, Yu MB, ShiYang Z *et al*. 25 GHz operation of silicon optical modulator with projection MOS structure. In: Optical Fiber Communication Conference; 21–25 March, 2010. San Diego, CA, USA. OSA, 2010; doi:10.1364/OFC.2010.OMI3.
- 4 Green WM, Rooks MJ, Sekaric L, Vlasov YA. Ultra-compact, low RF power, 10 Gb/s silicon Mach–Zehnder modulator. *Opt Express* 2007; **15**: 17106–17113.
- 5 Baba T, Akiyama S, Imai M, Akagawa T, Takahashi M *et al*. 25-Gbps operation of silicon p–i–n Mach–Zehnder optical modulator with 100- $\mu\text{m}$ -long phase shifter. In: CLEO: Science and Innovations; 6–11 May 2012. San Diego, CA, USA. IEEE, 2012.
- 6 Thomson DJ, Gardes FY, Fedeli JM, Zlatanovic S, Hu Y *et al*. 50-Gb/s silicon optical modulator. *IEEE Photon Technol Lett* 2012; **24**: 234–236.
- 7 Baehr-Jones T, Ding R, Liu Y, Ayazi A, Pinguet T *et al*. Ultralarge drive voltage silicon traveling-wave modulator. *Opt Express* 2012; **20**: 12014–12020.
- 8 Watts MR, Zortman WA, Trotter DC, Young RW, Lentine AL. Vertical junction silicon microdisk modulators and switches. *Opt Express* 2011; **19**: 21989–22003.
- 9 Almeida VR, Xu Q, Barrios CA, Lipson M. Guiding and confining light in void nanostructure. *Opt Lett* 2004; **29**: 1209–1211.
- 10 Baehr-Jones TW, Hochberg MJ. Polymer silicon hybrid systems: a platform for practical nonlinear optics. *J Phys Chem C* 2008; **112**: 8085–8090.
- 11 Leuthold J, Freude W, Brosi JM, Baets R, Dumon P *et al*. Silicon organic hybrid technology—a platform for practical nonlinear optics. *Proc IEEE* 2009; **97**: 1304–1316.
- 12 Dalton LR, Sullivan PA, Bale DH. Electric field poled organic electro-optic materials: state of the art and future prospects. *Chem Rev* 2010; **110**: 25–55.
- 13 Brosi JM, Koos C, Andreani LC, Waldow M, Leuthold J *et al*. High-speed low-voltage electro-optic modulator with a polymer-infiltrated silicon photonic crystal waveguide. *Opt Express* 2008; **16**: 4177–4191.
- 14 Hochberg M, Baehr-Jones T, Wang G, Huang J, Sullivan P *et al*. Towards a millivolt optical modulator with nano-slot waveguides. *Opt Express* 2007; **15**: 8401–8410.
- 15 Baehr-Jones T, Penkov B, Huang J, Sullivan P, Davies J *et al*. Nonlinear polymer-clad silicon slot waveguide modulator with a half wave voltage of 0.25 V. *Appl Phys Lett* 2008; **92**: 163303.
- 16 Wülbern JH, Prorok S, Hampe J, Petrov A, Eich M *et al*. 40 GHz electro-optic modulation in hybrid silicon–organic slotted photonic crystal waveguides. *Opt Lett* 2010; **35**: 2753–2755.
- 17 Alloati L, Korn D, Palmer R, Hillerkuss D, Li J *et al*. 42.7 Gbit/s electro-optic modulator in silicon technology. *Opt Express* 2011; **19**: 11841–11851.
- 18 Ding R, Baehr-Jones T, Liu Y, Bojko R, Witzens J *et al*. Demonstration of a low  $V_\pi L$  modulator with GHz bandwidth based on electro-optic polymer-clad silicon slot waveguides. *Opt Express* 2010; **18**: 15618–15623.
- 19 Palmer R, Alloati L, Korn D, Schindler PC, Baier M *et al*. Low power Mach–Zehnder modulator in silicon–organic hybrid technology. *IEEE Photon Technol Lett* 2013; **25**: 1226–1229.
- 20 Palmer R, Alloati L, Korn D, Heni W, Schindler PC *et al*. Low-loss silicon strip-to-slot mode converters. *IEEE Photon J* 2013; **5**: 2200409.
- 21 Korn D, Palmer R, Yu H, Schindler PC, Alloati L *et al*. Silicon–organic hybrid (SOH) IQ modulator using the linear electro-optic effect for transmitting 16QAM at 112 Gbit/s. *Opt Express* 2013; **21**: 13219–13227.
- 22 Elder DL, Benight SJ, Song J, Robinson BH, Dalton LR. Matrix-assisted poling of monolithic bridge-disubstituted organic NLO chromophores. *Chem Mater* 2014; **26**: 872–874.
- 23 Ding R, Baehr-Jones T, Kim WJ, Spott A, Fournier M *et al*. Sub-volt silicon–organic electro-optic modulator with 500 MHz bandwidth. *J Lightwave Technol* 2011; **29**: 1112–1117.
- 24 Takayesu J, Hochberg M, Baehr-Jones T, Chan E, Wang GX *et al*. A hybrid electrooptic microring resonator-based  $1 \times 4 \times 1$  ROADM for wafer scale optical interconnects. *J Lightwave Technol* 2009; **27**: 440–448.
- 25 Gould M, Baehr-Jones T, Ding R, Huang S, Luo J *et al*. Silicon–polymer hybrid slot waveguide ring-resonator modulator. *Opt Express* 2011; **19**: 3952–3961.
- 26 Wang X, Lin CY, Chakravarty S, Luo J, Jen AKY *et al*. Effective in-device  $r_{33}$  of 735 pm/V on electro-optic polymer infiltrated silicon photonic crystal slot waveguides. *Opt Lett* 2011; **36**: 882–884.
- 27 Palmer R, Koerber S, Heni W, Elder DL, Korn D *et al*. High-speed silicon–organic hybrid (SOH) modulator with 1.6 fJ/bit and 180 pm/V in-device nonlinearity. In: Proceedings of the 39th European Conference and Exhibition on Optical Communication (ECOC 2013). IET, 2013.
- 28 Taillaert D, van Laere F, Ayre M, Bogaerts W, van Thourhout D *et al*. Grating couplers for coupling between optical fibers and nanophotonic waveguides. *Jpn J Appl Phys* 2006; **45**: 6071–6077.
- 29 Wolff JJ, Wortmann R. Organic materials for second-order non-linear optics. In: *Advances in Physical Organic Chemistry*. Oxford: Elsevier; 1999. p121–217.
- 30 Dalton LR, Benight SJ, Johnson LE, Knorr DB, Kosilkin I *et al*. Systematic nanoengineering of soft matter organic electro-optic materials. *Chem Mater* 2011; **23**: 430–445.
- 31 Dalton LR, Sullivan PA, Bale D, Olbricht B, Davies J *et al*. Organic electro-optic materials. In: *Organic Thin Films for Photonic Applications*. Washington, DC: American Chemical Society; 2010. p13–33.

- 32 Baehr-Jones T, Hochberg M, Wang G, Lawson R, Liao Y *et al*. Optical modulation and detection in slotted silicon waveguides. *Opt Express* 2005; **13**: 5216–5226.
- 33 Huang S, Luo J, Yip HL, Ayazi A, Zhou XH *et al*. Efficient poling of electro-optic polymers in thin films and silicon slot waveguides by detachable pyroelectric crystals. *Adv Mater* 2012; **24**: OP42–OP47.
- 34 Enami Y, Derosé CT, Mathine D, Loychik C, Greenlee C *et al*. Hybrid polymer/sol-gel waveguide modulators with exceptionally large electro-optic coefficients. *Nat Photonics* 2007; **1**: 180–185.
- 35 Benight SJ, Johnson LE, Barnes R, Olbricht BC, Bale DH *et al*. Reduced dimensionality in organic electro-optic materials: theory and defined order. *J Phys Chem B* 2010; **114**: 11949–11956.
- 36 Dalton LR, Lao D, Olbricht BC, Benight S, Bale DH *et al*. Theory-inspired development of new nonlinear optical materials and their integration into silicon photonic circuits and devices. *Opt Mater* 2010; **32**: 658–668.
- 37 Palmer R, Koeber S, Elder DL, Woessner M, Heni W *et al*. High-speed, low drive-voltage silicon-organic hybrid modulator based on a binary-chromophore electro-optic material. *J Lightwave Technol* 2014; **32**: 2726–2734.
- 38 Dong P, Chen L, Chen YK. High-speed low-voltage single-drive push-pull silicon Mach-Zehnder modulators. *Opt Express* 2012; **20**: 6163–6169.
- 39 Leuthold J, Koos C, Freude W, Alloatti L, Palmer R *et al*. Silicon-organic hybrid electro-optical devices. *IEEE J Sel Top Quantum Electron* 2013; **19**: 3401413.
- 40 Chang F, Onohara K, Mizuochi T. Forward error correction for 100 G transport networks. *IEEE Commun Mag* 2010; **48**: S48–S55.
- 41 Luo J, Huang S, Shi Z, Polishak BM, Zhou XH *et al*. Tailored organic electro-optic materials and their hybrid systems for device applications. *Chem Mater* 2011; **23**: 544–553.
- 42 Shi Z, Liang W, Luo J, Huang S, Polishak BM *et al*. Tuning the kinetics and energetics of Diels-Alder cycloaddition reactions to improve poling efficiency and thermal stability of high-temperature cross-linked electro-optic polymers. *Chem Mater* 2010; **22**: 5601–5608.
- 43 Huang W, Jin Z, Shi Z, Intemann JJ, Li M *et al*. Spontaneous thermal crosslinking of a sydnone-containing side-chain polymer with maleimides through a convergent [3 + 2] dual cycloaddition/cycloreversion process for electro-optics. *Polym Chem* 2013; **4**: 5760–5767.
- 44 Shi Z, Luo J, Huang S, Polishak BM, Zhou XH *et al*. Achieving excellent electro-optic activity and thermal stability in poled polymers through an expeditious crosslinking process. *J Mater Chem* 2012; **22**: 951–959.



This work is licensed under a Creative Commons Attribution-NonCommercial-NoDerivs 3.0 Unported License. The images or other third party material in this article are included in the article's Creative Commons license, unless indicated otherwise in the credit line; if the material is not included under the Creative Commons license, users will need to obtain permission from the license holder to reproduce the material. To view a copy of this license, visit <http://creativecommons.org/licenses/by-nc-nd/3.0/>

Supplementary information for this article can be found on the *Light: Science & Applications*' website (<http://www.nature.com/lisa/>).